P_2

C R - 134519

ENGINEERING AND INDUSTRIAL EXPERIMENT STATION

College of Engineering

University of Florida

Gainesville

MASS TRANSFER IN FUEL CELLS

Prepared for
National Aeronautics and Space Administration
Washington, D.C.

September 26, 1973

Robert D. Walker

Robert D. Walker, Jr.

ENGINEERING AND INDUSTRIAL EXPERIMENT STATION

College of Engineering
University of Florida
Gainesville, Florida

I

TABLE OF CONTENTS

LIST OF TABLES

LIST OF FIGURES

1. Summary

This report describes the results of experiments on electron microscopy of fuel cell components, thermal decomposition of Teflon by thermogravimetry, surface area and pore size distribution measurements, water transport in fuel cells, and surface tension of KOH solutions.

Scanning electron microscopy was found to give satisfactory characterization of the gross features of fuel cell electrodes and of electrolyte matrices. However, the resolution of this process was inadequate to reveal the details of electrode structure. Transmission electron microscopy of thin (50 nm) sections of impregnated electrodes has successfully revealed the crystallite and agglomerate sizes of the catalyst, but it is attended with great difficulty and has not yet revealed the presence of Teflon.

Thermogravimetric analysis has demonstrated that substantially all of the Teflon in a catalyst--Teflon suspension is retained with the catalyst, and that Teflon decomposes thermally at a lower temperature in the presence of the catalyst than is the case where no catalyst is present.

Surface area and pore size distribution measurements by nitrogen adsorption and mercury porosimetry have revealed that electrodes have several preferred radii for pores, the smallest being about 2.5 nm (25 A)--which is near the size of the crystallites of the catalyst. A computer program for automatically analyzing pore size distribution data and generating a listing of preferred mean pore radii has been written and tested on data from an Englehard fuel cell grade platinum black and on two P & W fuel cell electrodes.

1

Water transport in fuel cells has been considered and the influence of ionic hydration has been demonstrated to be of considerable importance. Hydration number and transference number data for concentrated KOH solutions are very scarce, however, and accurate measurements of both parameters are required before water transport can be dealt with precisely.

A literature survey of KOH surface properties reveals that there are no experimental data for concentrated KOH solutions and temperatures above 18°C. Experimental measurements of the surface tension will be undertaken, and wetting and penetration of porous, heterogeneous surfaces by concentrated KOH solutions will be studied.

2. Electron Microscopy--V. M. Jalan

Both scanning and transmission electron microscopy have been employed in studies concerned with a more adequate understanding of the influence of physical structures on the behavior of fuel cell components, and both successes and failure have been experienced.

2.1 Electron Microscopy of Electrolyte Matrix Materials

Scanning electron microscopy was successfully applied to a study of several samples of electrolyte matrix. These matrices were made either from asbestos--in some cases reconstituted--or from Fybex (DuPont fibrous potassium titanate). Scanning electron micrographs of three samples of asbestos electrolyte matrix materials at 1800X magnification are shown in Figure 1, and electron micrographs of these same materials at 9000X magnification are shown in Figure 2. Scanning electron micrographs of two samples of Fybex electrolyte matrices at 1800X and 9000X magnification are shown in Figure 3.

It can be seen from Figures 1 and 2 that the fiber bundles in the electrolyte matrix labeled Johns-Manville Asbestos are not as well separated as are the fiber bundles in the two matrix samples labeled Reconstituted Asbestos. Clearly the additional processing has improved fiber bundle separation and fiber dispersion. These electron micrographs reveal that the individual asbestos fibers are about 0.01 μm (100 A) in diameter and perhaps a millimeter in length. The individual fibers--and even fairly massive fiber bundles--are clearly quite flexible.

Figure 1: Scanning Electron Micrographs of Asbestos Electrolyte
Matrices. Magnification: 1800X

Asbestos-1 (John Mansville)
1800X
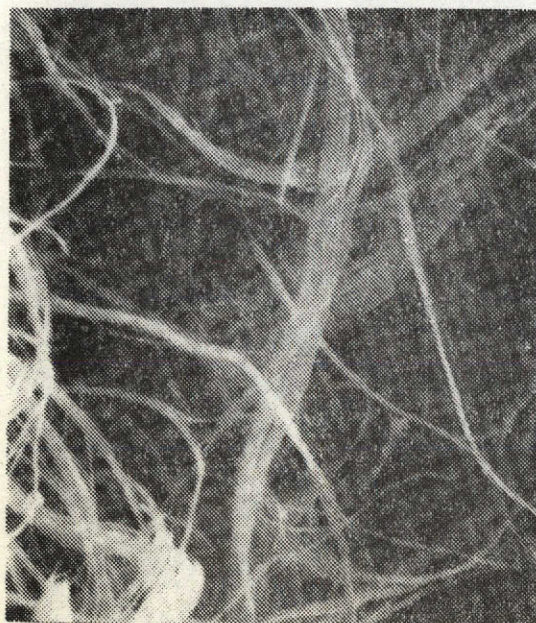
Asbestos-2 (Reconstituted)
1800X

Asbestos-3 (Reconstituted)
1800X

Figure 2: Scanning Electron Micrographs of Asbestos Electrolyte
Matrices. Magnification: 9000X

Asbestos-1 (John Mansville)

9000X
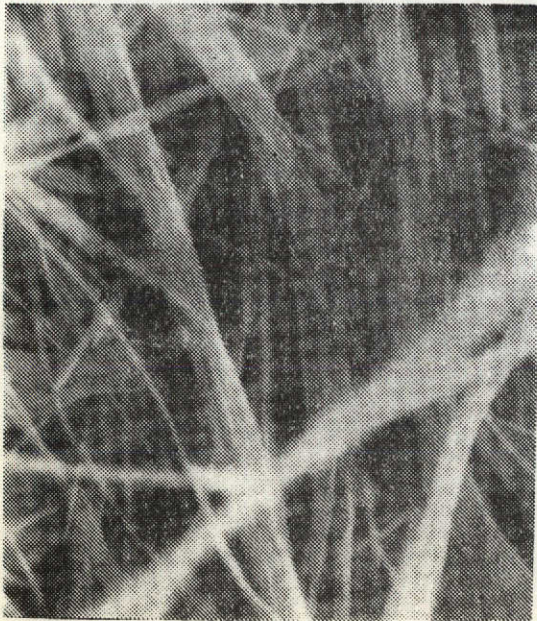
Asbestos-2 (Reconstituted)

9000X

Asbestos-3 (Reconstituted)

9000X

In contrast to asbestos, Figure 3 reveals that Fybex, in the samples examined, is relatively completely dispersed as single fibers. As compared to asbestos, Fybex fibers are 1) much larger in diameter (0.2 μm vs 0.01 μm), 2) much shorter (5-10 μm vs 50 μm or more), and 3) less flexible, It also appears that Fybex fibers are more easily shortened by breaking during processing than asbestos fibers.

2.2 Electron Microscopy of Electrode Materials

It may be recalled that scanning electron microscopy (SEM) had been found useful for gross examination of electrode materials, particularly for surface roughness, but only transmission electron microscopy (TEM) yielded micrographs which revealed details of the electrode structure. Even though TEM revealed substantial detail in the catalyst aggregates, it failed to detect the presence of Teflon-- a constituent which should occupy roughly one-half of the volume of the catalyst layer. In spite of several variations in the technique of impregnation of electrode samples, no good sections were obtained. The apparently weak bond between Teflon and the epoxy resin which was used to impregnate the samples may be the source of much of the difficulty. Many tears appeared in the thin (about 50 nanometers thick) sections which were obtained from the microtome. In any event, it seems unlikely that every Teflon particle would have been torn out of the impregnated sample, but no areas on the electron micrographs could be associated with Teflon. Experiments employing negative staining are planned for the near future, and thermogravimetry will be employed to ascertain the presence of Teflon in the catalyst layer.

Figure 3: Scanning Electron Micrographs of Fybex Electrolyte Matrices.
Magnification: 1800X and 9000X.
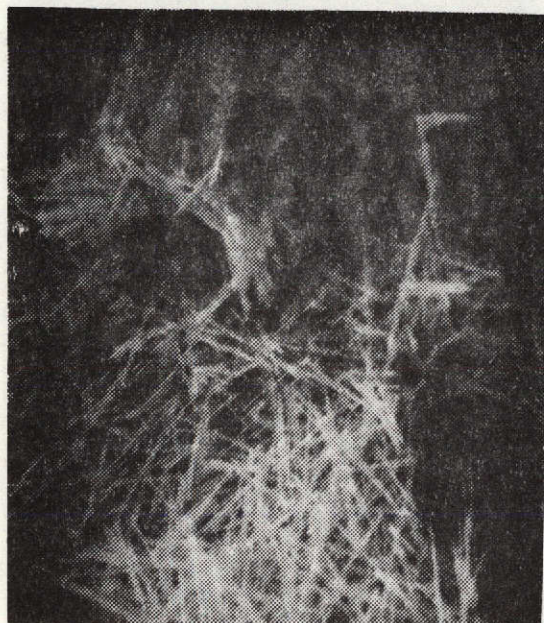
Fybex-1 1800X

Fybex-1 9000X
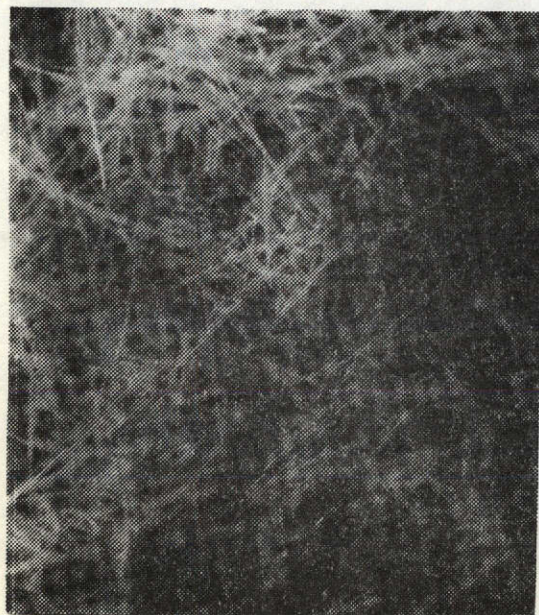
Fybex-2 1800X
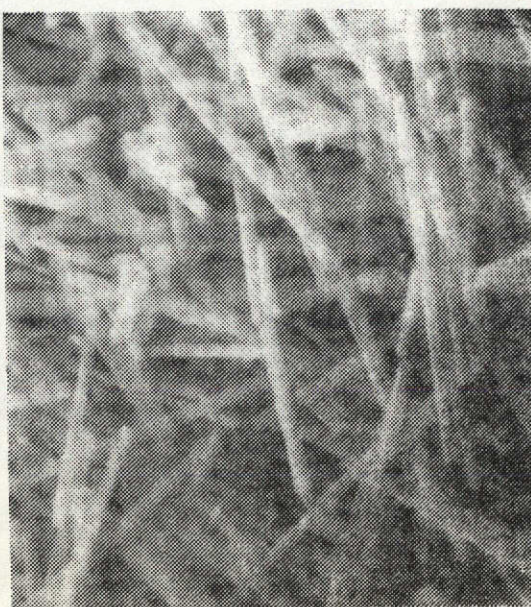
Fybex-2 9000X

3. Thermogravimetric Analysis – V. M. Jalan

As reported previously and also found in early this work period, all electron microscopy efforts showed no evidence of Teflon particles in the catalyst layer of the electrodes. Indeed, if the catalyst layer contained 20 weight percent Teflon, one would expect to find roughly one-half of the volume to be occupied by Teflon. Our failure to see evidence of the presence of Teflon in the electron micrographs raised questions as to the actual amount of Teflon present in the electrode. We reasoned that, perhaps, a part of the Teflon was lost in the filterate during fabrication of the electrode and a part could have been lost during high temperature sintering in the presence of Pt black catalyst.

To check for the actual amount of Teflon present in the electrode, thermogravimetric analyses were made on Pt black catalyst powder, air-dried Teflon, air-dried Teflon-catalyst mixture, sintered Teflon, sintered Teflon-catalyst mixture, and a sample taken from a P & W fuel cell electrode.

As expected no loss in weight was detected in the catalyst while a small amount of residue remained after Teflon decomposed. Air-dried Teflon lost about 6% weight at around 200°C, which we believe is due to burning of the wetting agent (Tritan X-100), then it started decomposing at 480°C. All the Teflon was lost by 610°C as shown in Figure 4. The decomposition temperature range of 480°C - 610°C remains unchanged even for sintered Teflon as seen in Figure 5. However, it is interesting to note that in the presence of Pt black catalyst loss of Teflon occured between 400 - 540°C (See Figure 6). This, we believe, is due to catalysed decomposition of Teflon. On Pt/Pd - Teflon electrodes the decomposition temperature range is
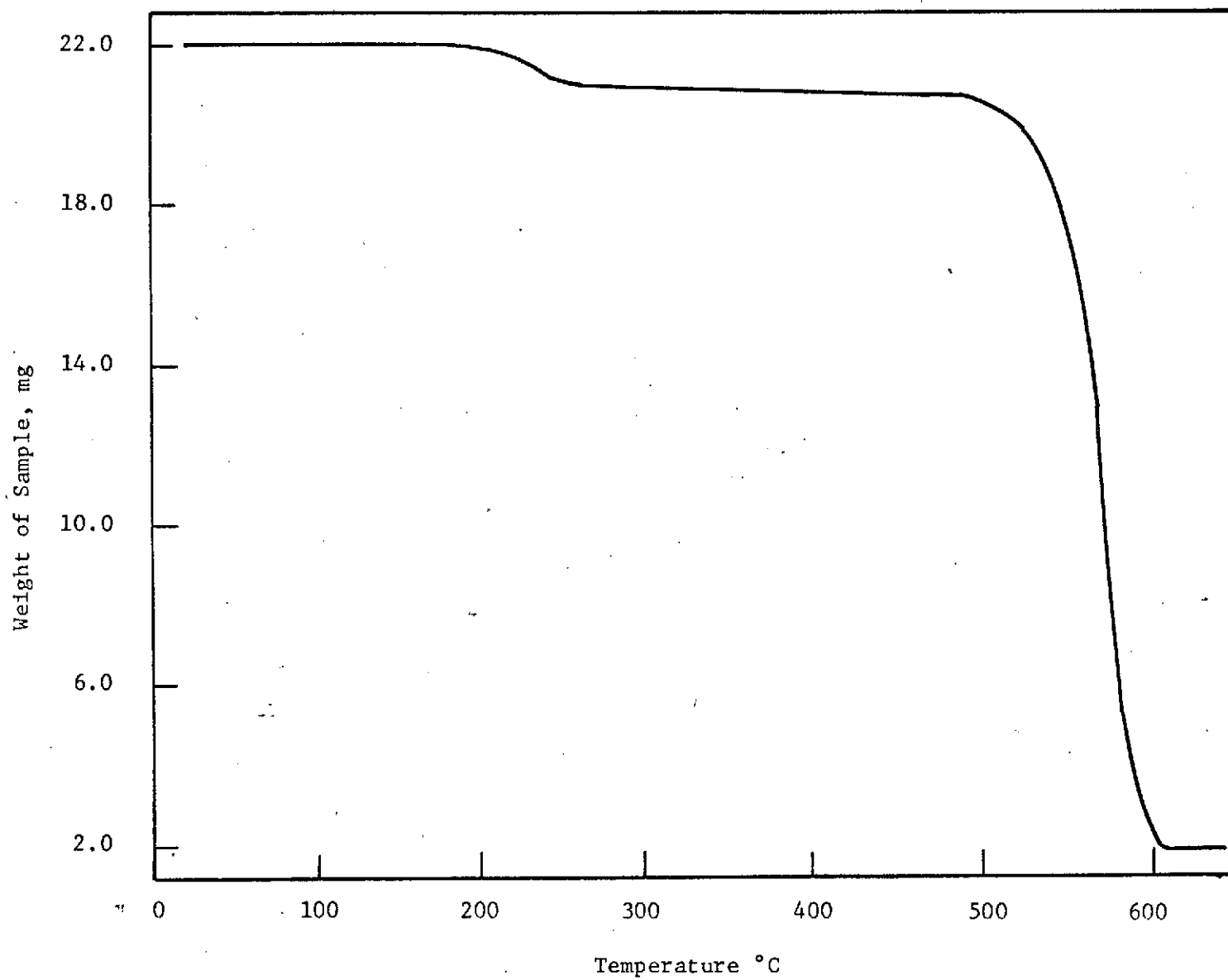
Figure 4. Thermogravimetric Analysis of Teflon-30
(Dried at room temperature under argon atmosphere)
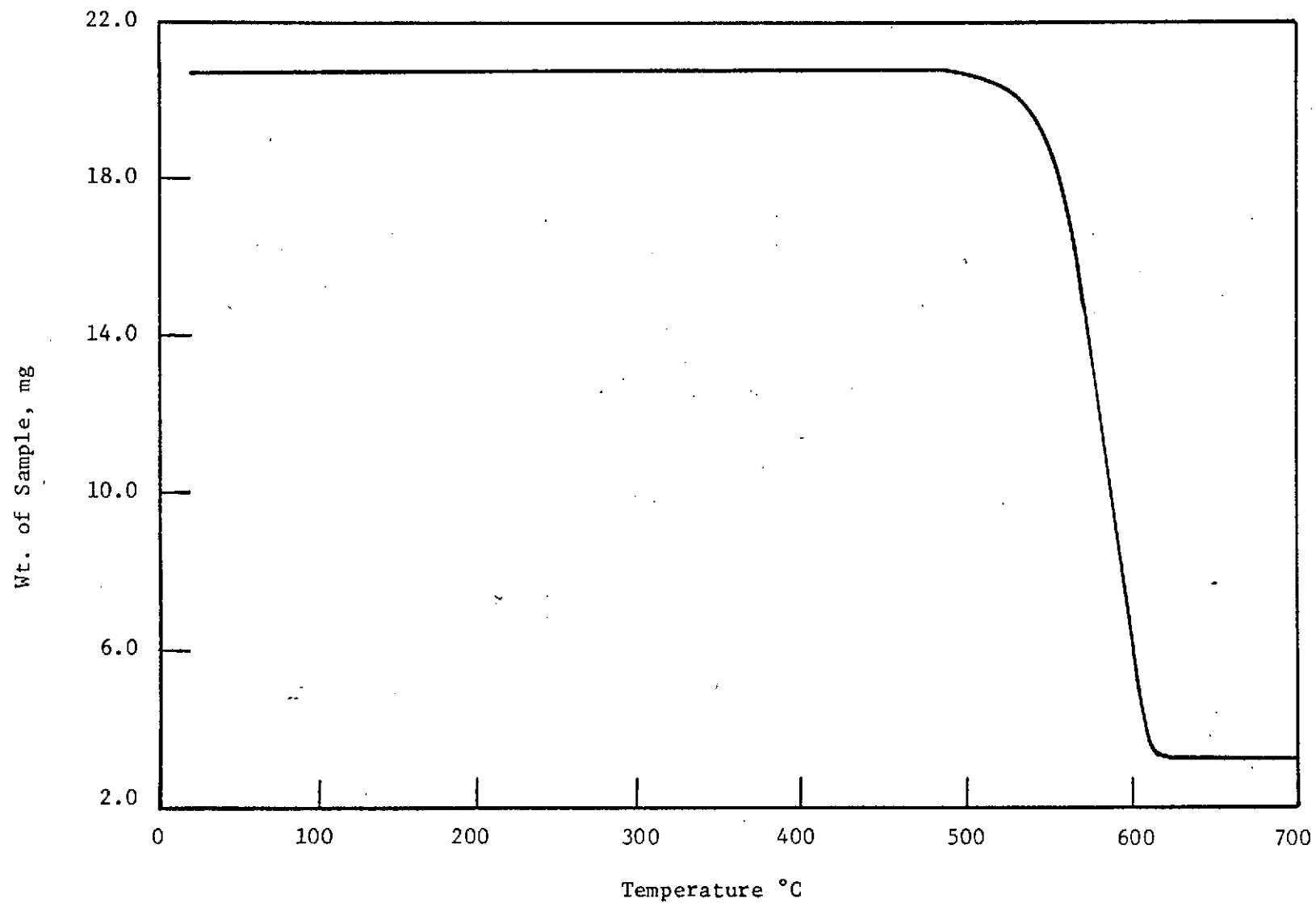
Figure 5. Thermogravimetric of Teflon-30 Sample
(Sintered for 15 minutes at 310°C under Argon atmosphere)
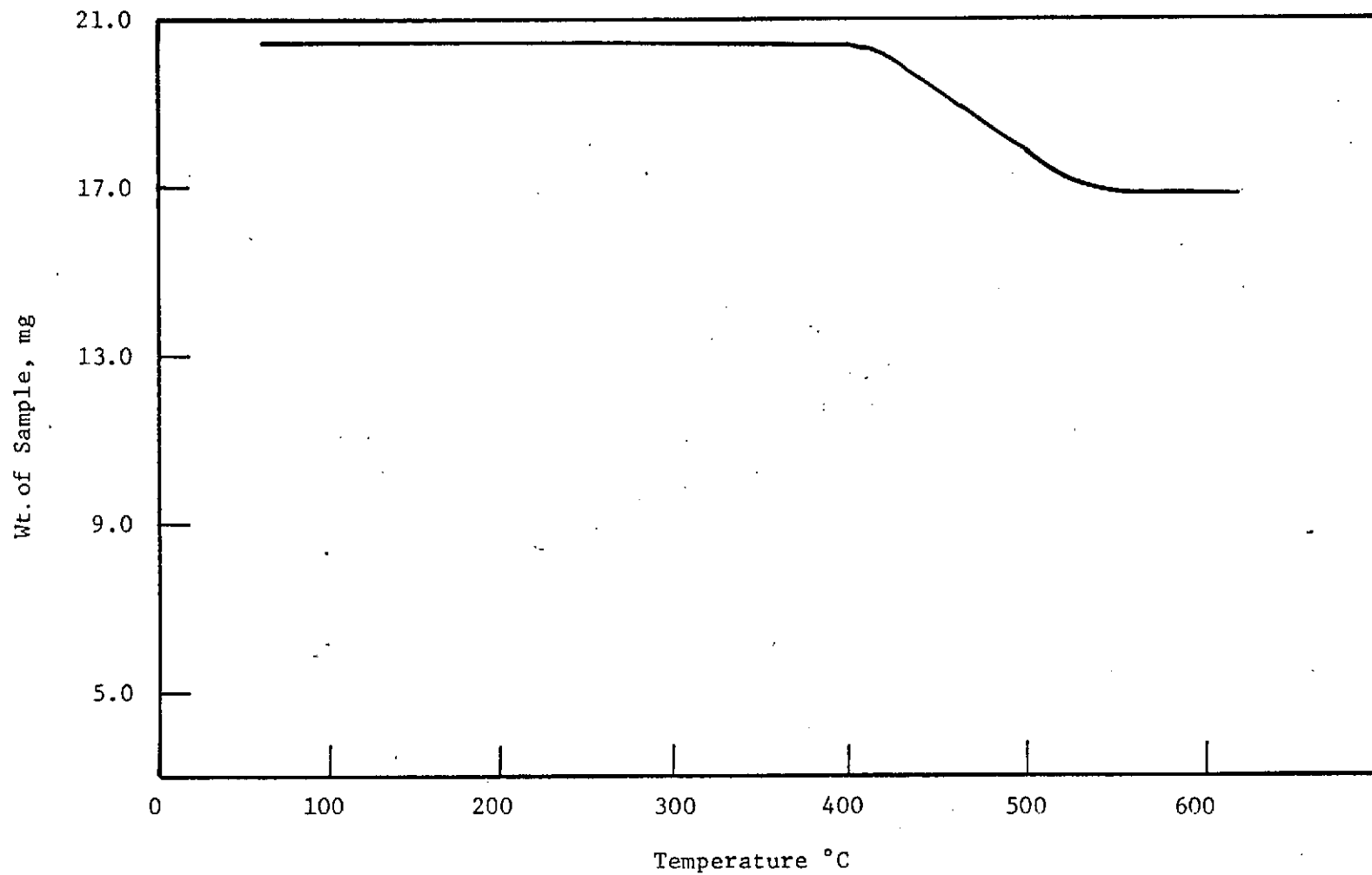
Figure 6. Thermogravimetric Analysis of Sample containing
Pt, black and Teflon 30 (Sintered for 15 minutes at 310°C under Argon atmosphere).

further reduced to 340 - 510°C as shown in Figure 7 indicating a stronger catalytic effect of Pt/Pd catalyst.

Assuming that all the weight loss is due to Teflon we found the electrode to contain 2.2 to 2.5 mg of Teflon per sq. cm of electrode. Considering that the electrode has a catalyst loading of about 10 mg/cm^2 this checks out the Teflon content to be about 25 percent of the catalyst loading.

Once set up, the ease and precision of thermogravimetric analysis suggest the usefulness of the technique for quality control of the Teflon content of fabricated electrodes.

Thermogravimetric analysis of Fybex and asbestos electrolyte matrices showed that Fybex lost no weight up to 700°C--as expected, but the weight losses of the asbestos sample are not in complete agreement with the expected weight loss--at least for chrysotile asbestos. This point may warrant further investigation.
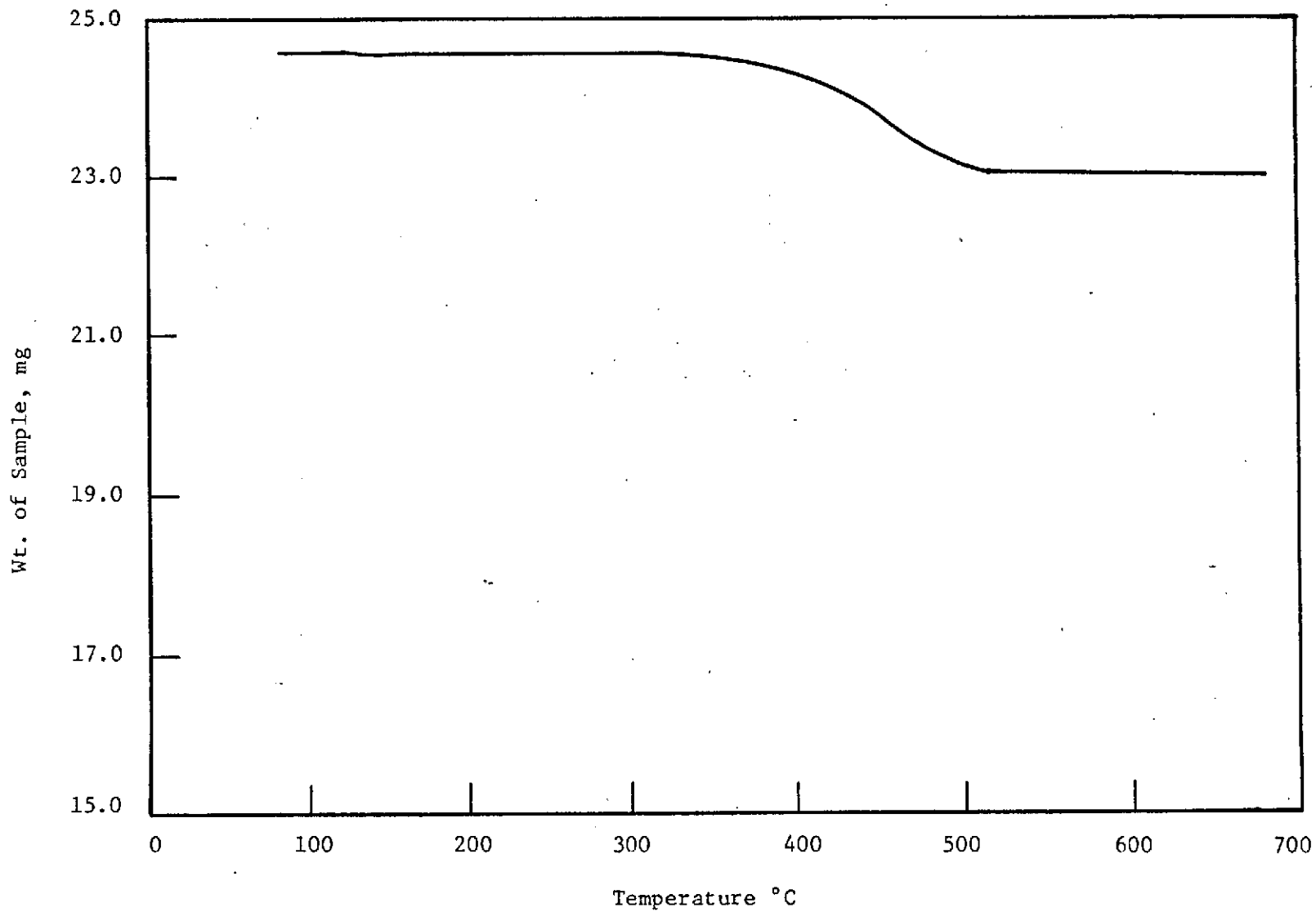
Figure 7. Thermogravimetric Analysis of P & W Fuel Cell
Electrode (Pt/Pd – Teflon on Ni Screen)

13

4. Surface Area and Pore Size Distribution Measurements
   M. C. Lee and V. M. Jalan

4.1 Discussion of Methods

4.1.1 Surface Area Measurements

BET measurement was the technique which was used for measuring

the surface areas of fuel cell electrodes, electrolyte separator

materials, and platinum catalyst. This method involves measuring the

amount of gas adsorbed on a solid surface at a temperature close to the

boiling point of the gas. A quantity of sample is weighed into the

sample cell and pretreated for about 18 hours at 200-220°C while a

stream of pure helium flows through the cell to remove moisture and

other contaminants. After pretreatment the sample is reweighed to

determine the dry weight.

In the continuous flow method nitrogen is used as the adsorbate

and helium is used as the carrier gas. A mixture of nitrogen and

helium of known composition is passed through the sample and the

effluent composition is monitored by thermal conductivity measurements.

When the sample is cooled in liquid nitrogen, the adsorption of

nitrogen is indicated by a peak on a recorder chart. After adsorption

equilibrium is established, the recorder pen returns to its original

baseline. The sample tube is allowed to warm by removing the liquid

nitrogen coolant, causing desorption of nitrogen and producing a peak on

the chart which is in the reverse direction of the adsorption peak. The

area under the desorption peak is a measure of the nitrogen adsorbed.

This peak area was calibrated by injecting a known amount of nitrogen

into the nitrogen-helium stream to give a peak of similar magnitude to

the area of the desorption peak. The amount of nitrogen adsorbed is calculated by comparing these two peak areas. Adsorption, desorption and calibration are done at several relative nitrogen pressure ratios in the range from 0.05 to 0.3.

After computing the amount of nitrogen adsorbed and the corresponding relative pressures, the amount of nitrogen adsorbed in a monolayer, V_m, is determined from the BET equation:

$$\frac{P}{V_{ads}(P_o - P)} = \frac{C - 1}{V_m C} \frac{P}{P_o} + \frac{1}{V_m C} \tag{1}$$

where

> P: partial pressure of the adsorption gas
>
> P_o: saturation pressure of the adsorption gas over the solid sample at the temperature of coolant
>
> V_{ads}: total volume (STP) of adsorbed gas on the surface of of the adsorbent
>
> C: constant expressing the net adsorption energy
>
> V_m: volume (STP) of adsorbed gas when the entire adsorbent surface is covered with a monomolecular layer

When the left hand side of the equation is plotted as the ordinate versus the relative pressure, P/P_o, a straight line with slope $(C - 1)/V_m C$ and intercept $1/V_m C$ is obtained. If we note that

$$\frac{1}{\text{Slope + Intercept}} = \frac{1}{\frac{C-1}{V_m C} + \frac{1}{V_m C}} = \frac{V_m C}{C - 1 + 1} = V_m \tag{2}$$

then we can determine V_m from

$$V_m = \frac{1}{k_1 + k_2} \tag{3}$$

where k_1 is the slope and k_2 is the intercept of the straight line.
This value, multiplied by the proper factor for the area covered
per unit amount of nitrogen, gives the surface area, and when divided
by the dry weight of the sample, it yields the specific surface area.

4.1.2 Pore Size Distribution Measurements

The method used in measuring pore size distribution is an extension
of the original continuous flow method for the determination of surface
area. In surface area determinations low relative pressures of nitrogen
(P/P_o from 0.05 to 0.3) are used. Information on pore diameter and
pore volume can be obtained when the adsorption measurement is extended
to higher relative pressures of nitrogen (up to about 0.95).

The volume of gas desorbed is converted to a liquid volume per
gram of sample, and the Kelvin equation is used to give an estimate of
the diameter of the pores corresponding to the relative pressure of the
adsorbate above which no large pores are filled.

4.2 Experimental Results and Discussion

4.2.1 Decrease of Surface Area of Pt Black With Temperature of Pretreatment

Weighed samples of platinum catalyst (Englehard Fuel Cell Grade
Platinum Black) were heated in a stream of flowing helium for about 18
hours at temperatures ranging from 100°C to 400°C. Then the surface
area was measured as described in Section 4.1.1. Since it is standard
procedure to sinter fuel cell electrodes fabricated with platinum--
Teflon catalyst mixtures at a temperature between 310°C and 320°C,
surface area in the temperature range 300-350°C was studied carefully.
The data are shown in Table 1.

TABLE 1

Dependence of Surface Area on Pretreatment Temperature
Englehard Fuel Cell Platinum Black

Temp. of Pretreatment, °C	Surface Area, m^2/g
100	45.3
150	46.0
200	48.9
250	49.6
300	48.1
310	44.2
320	37.8
330	12.1
350	5.25
400	5.01

It is clear that a large decrease in surface area occurred when
the pretreating temperature was between 300°C and 350°C. A plot of
surface area versus pretreating temperature is shown in Figure 8. There
is a gradual increase in the surface area as the pretreating temperature
is increased to 200°C, but the slight changes in surface area between
200 and 300°C are probably not significant. There is a hint, however,
that reduction of surface area has already begun at 300°C, and the
advantages of sintering the Teflon at 310-320 must be weighed against
the loss in surface area. On the other hand the surface area lost on
sintering may be lost fairly early during the life of an electrode, and
it may not be significant for the entire life of a fuel cell.

Temperature of Pretreatment, °C
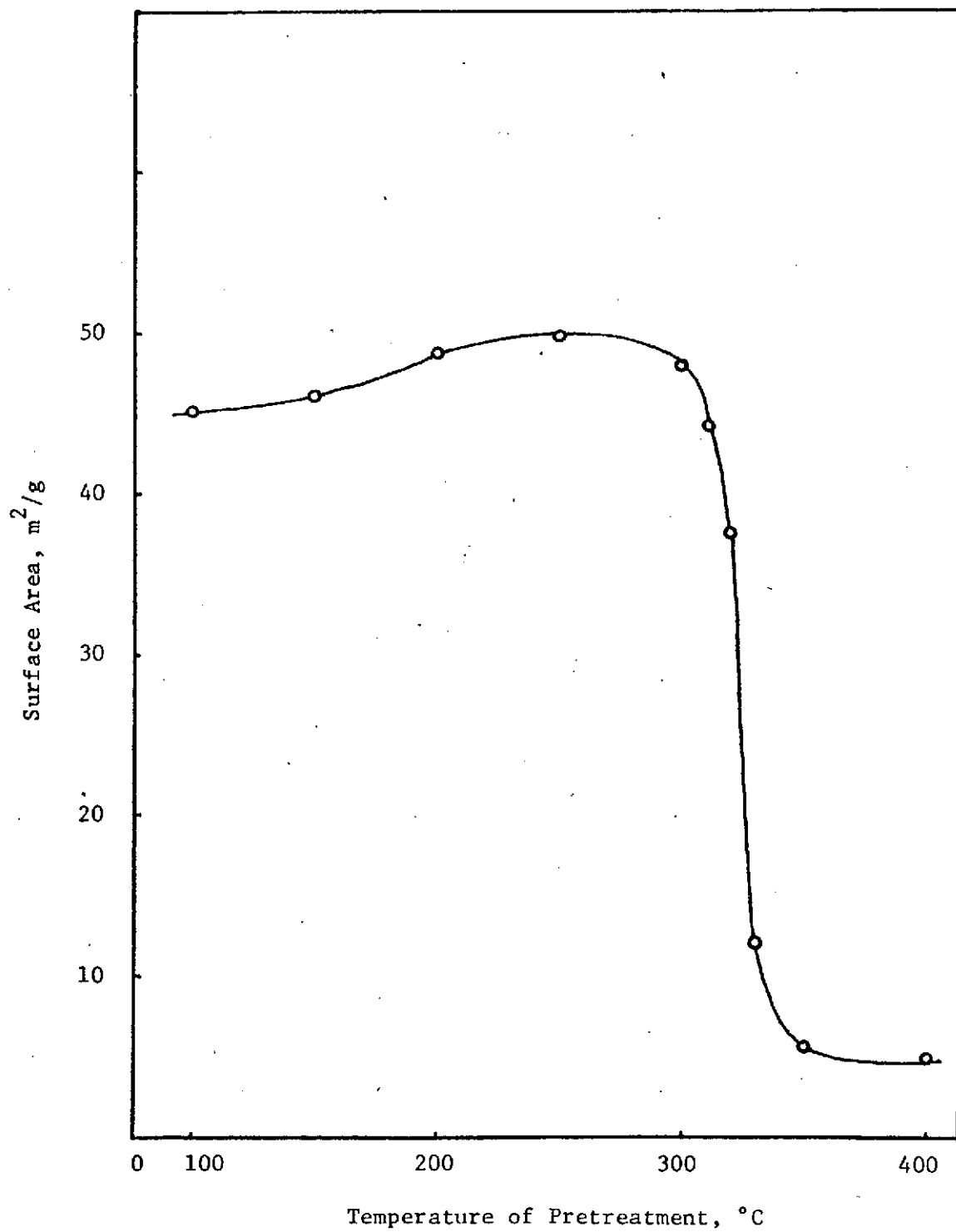
Dependence of Surface Area of Pt black on Pretreatment Temperature

Figure 8

4.2.2 Surface Area and Pore Size Distribution of Fuel Cell Components

4.2.2.1 Pratt and Whitney Fuel Cell Electrodes

The surface area and pore volumes of both the anode and the cathode from five Pratt and Whitney fuel Cells were measured. These fuel cells and the conditions to which they were subjected were described in a report issued in February, 1971 (1). The reader should refer to that report for full details, but certain factors are included in Table 2 to assist in analysis of the data. The pore size distribution curves in the pore size range up to about 35 nm are given in Figures 9-13.

It should be emphasized at the outset that the data in the table are taken on electrodes after testing. No samples before testing were available. Any conclusions must, therefore, be very tentative, and the principal value of these experiments is to demonstrate once again the usefulness of the surface area and pore size distribution test. Some observations do appear in order, however. First, the apparent pore volume test does not appear to yield useful information and, indeed, a review of the standard procedure makes it clear that this is not a particularly meaningful test as a variation of only a degree or two in the sample temperature (recall that it is at -191°C) would result in major differences in the apparent pore volume measured.

When the oxygen supply contained 4 ppm CO_2 and when the electrolyte matrix material was potassium titanate (PKT) the anode area was less than in the other fuel cells. The difference in surface area is not large, but it is measurable and it is reproducible. Therefore, the difference in anode surface area seems to be a real effect. Since we do not know what the original anode surface area was, we do have no way of determining whether this effect is particularly significant. Neither

Table 2

Surface Area and Pore Volume of Fuel Cell Electrodes

| P & W Cell Test Number	Fuel Cell Number	Cathode Material	Surface Area m^2/g		Apparent Pore Volume x10³ ml/g		Test Conditions	Remarks
			Anode	Cathode	Anode	Cathode		
1	SKN 44330 302320- 301782	Pt/Pd	1.12	1.90	10.2	13.6	30 mil Asb. 200 ASF	Thick Elec Matrix Avg. Cur. Dens. Cathode Visibly Worn
2	SKN 44728 302303- 301765	Pt/Pd	1.09	4.58	6.43	20.0	212 °F 200 ASF	T_{max} Cathode Avg. Cur. Dens.
6	SKN 49332 302348- 301810	Pt/Pd	0.89	4.02	6.54	13.0	4 ppm CO_2 PKT Matrix	CO_2 level Elec. Matrix Matl.
9	SKN 49334 302364- 301826	Pt/Pd	0.87	5.40	15.2	25.0	212 °F 4 ppm CO_2 30 mil PKT	T_{max} Cathode CO_2 level Matrix Thickness Matrix Matl.
Not Covered	SKN 49335 302375- 301837	Ag/Hg	1.10	1.78	7.42	5.09	No Information	No Information

20
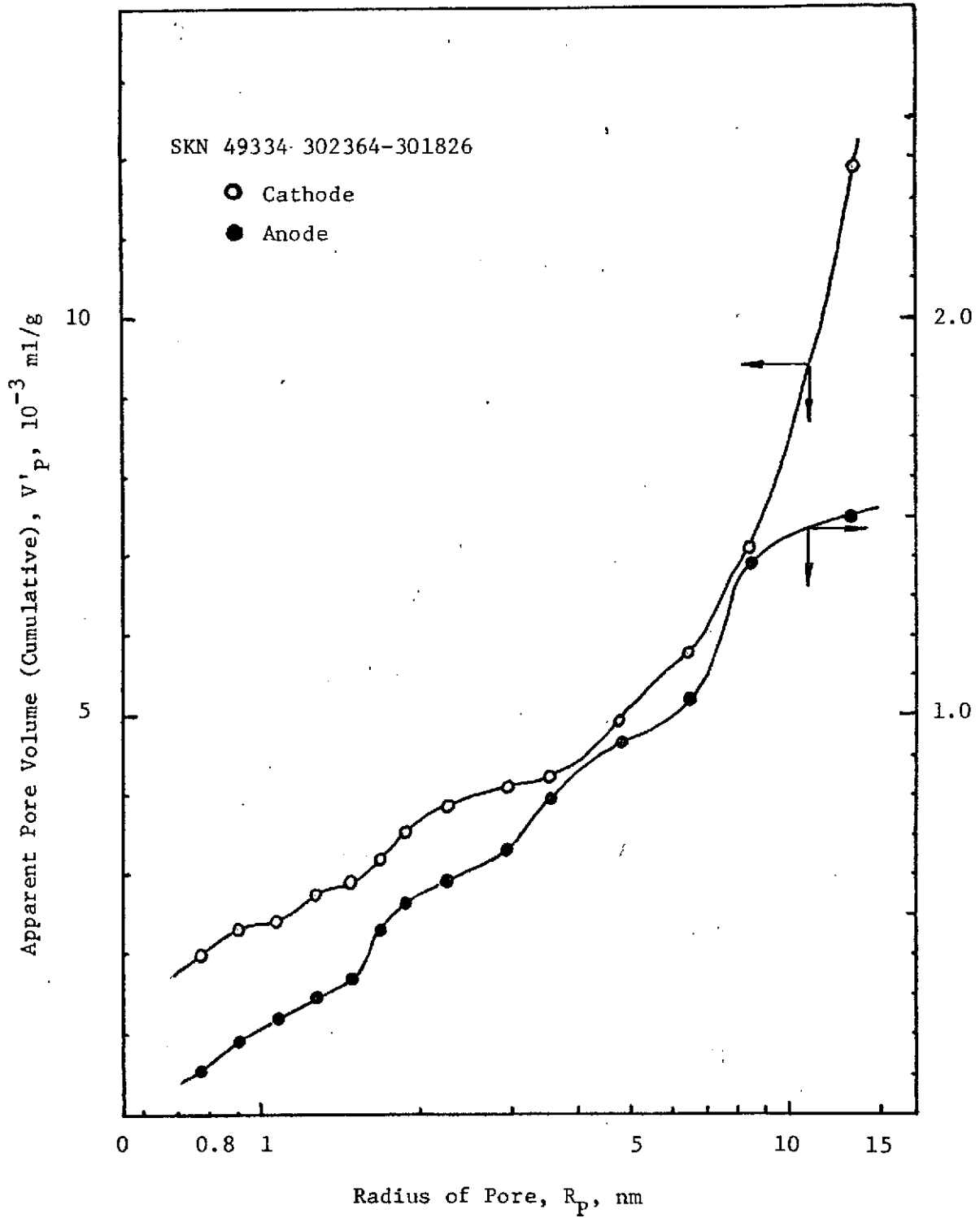
Figure 9

Pore Size Distribution of Electrode SKN 49334 302364-301826
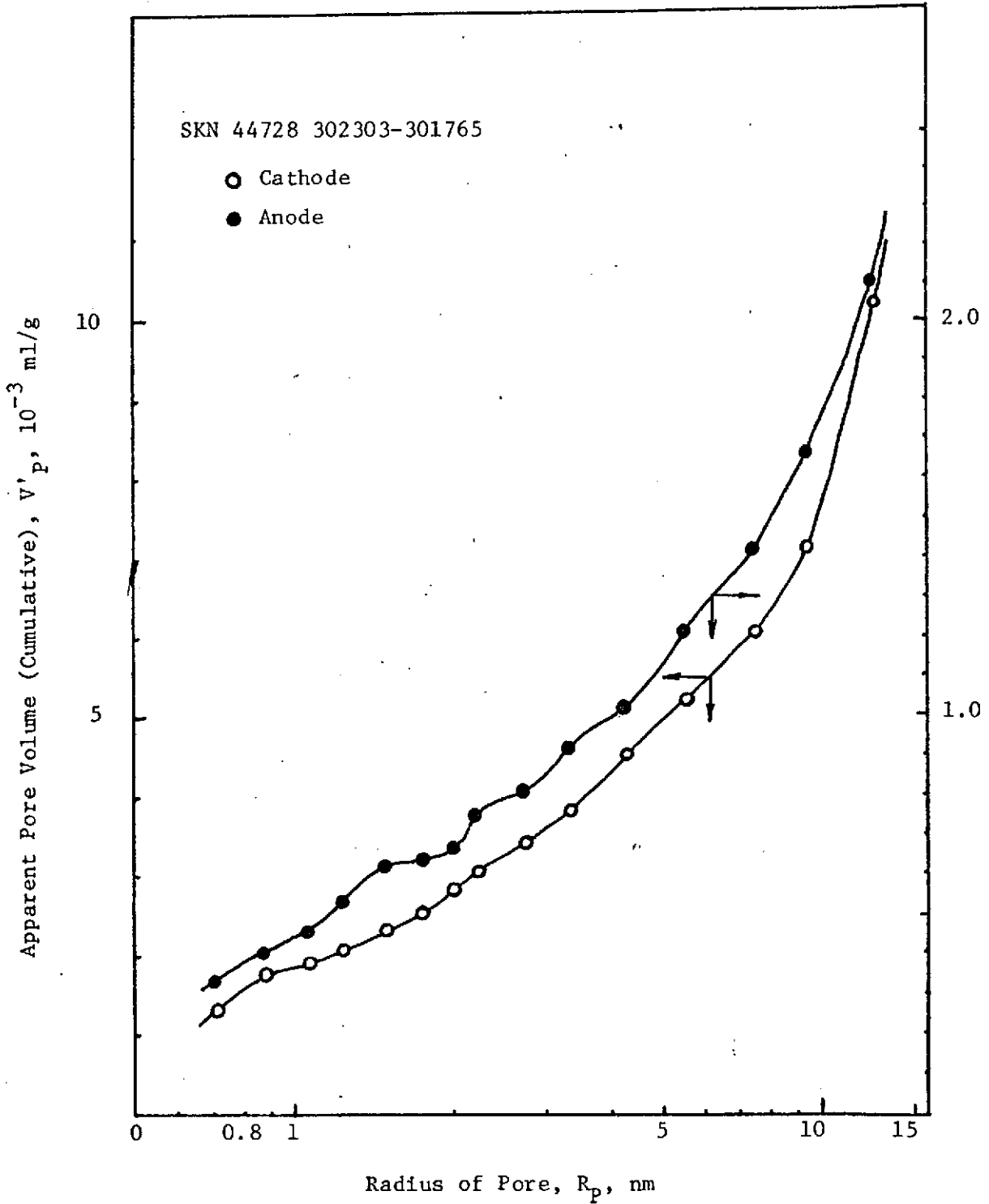
Figure 10

Pore Size Distribution of Electrode SKN 44728 302303-301765
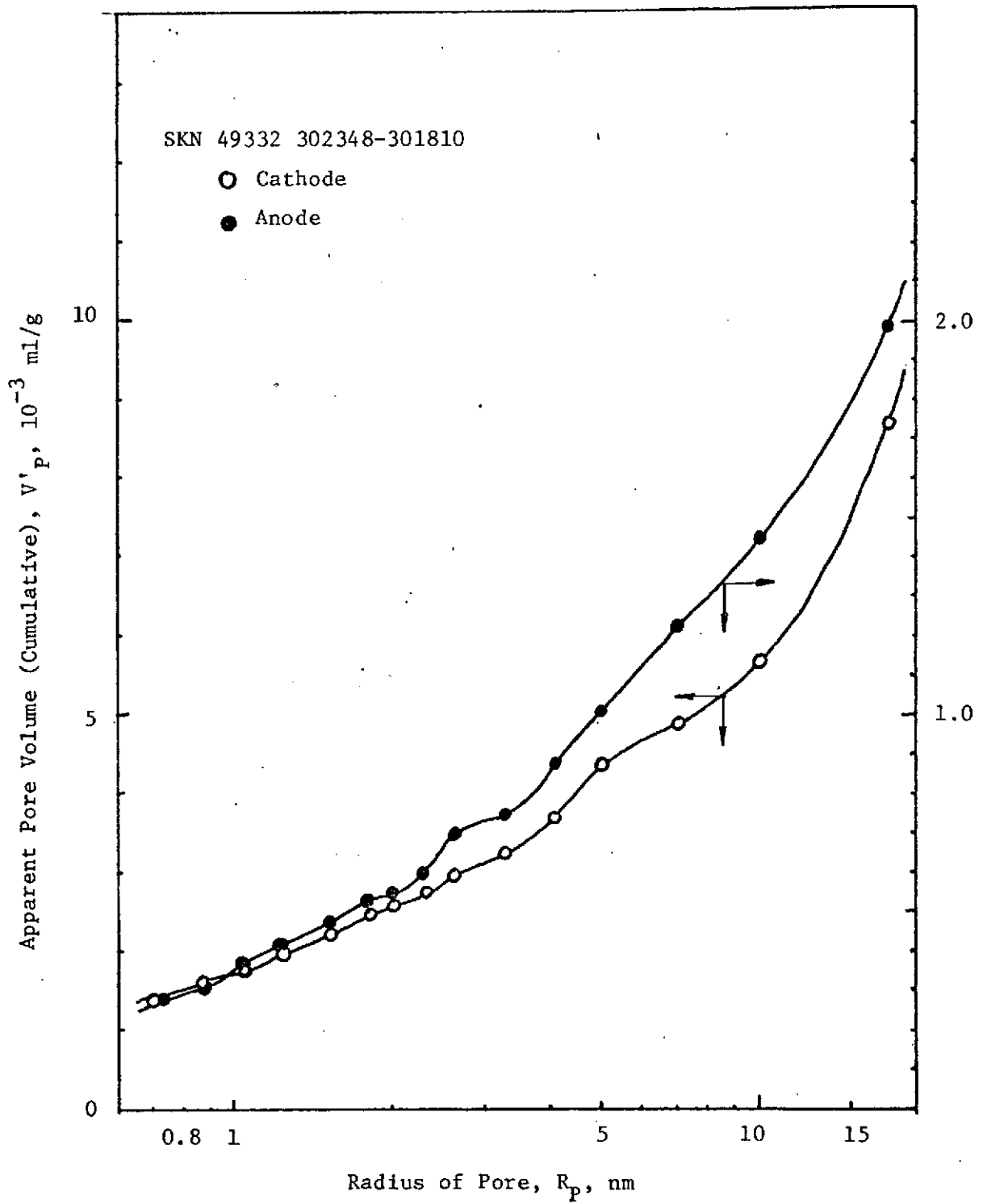
Figure 11

Pore Size Distribution of Electrode SKN 49332 302348-301810
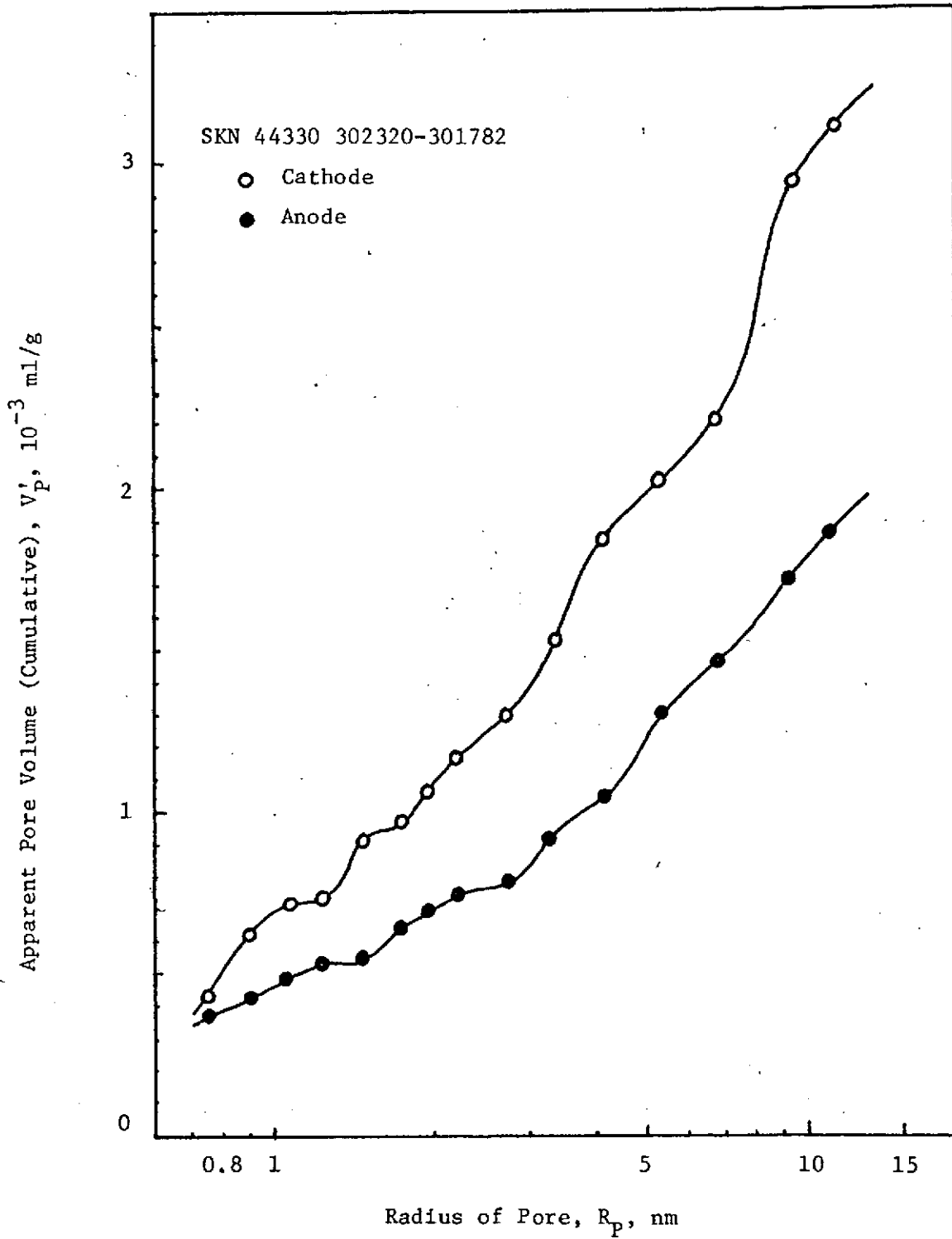
Figure 12

Pore Size Distribution of Electrode SKN 44330 302320-301782
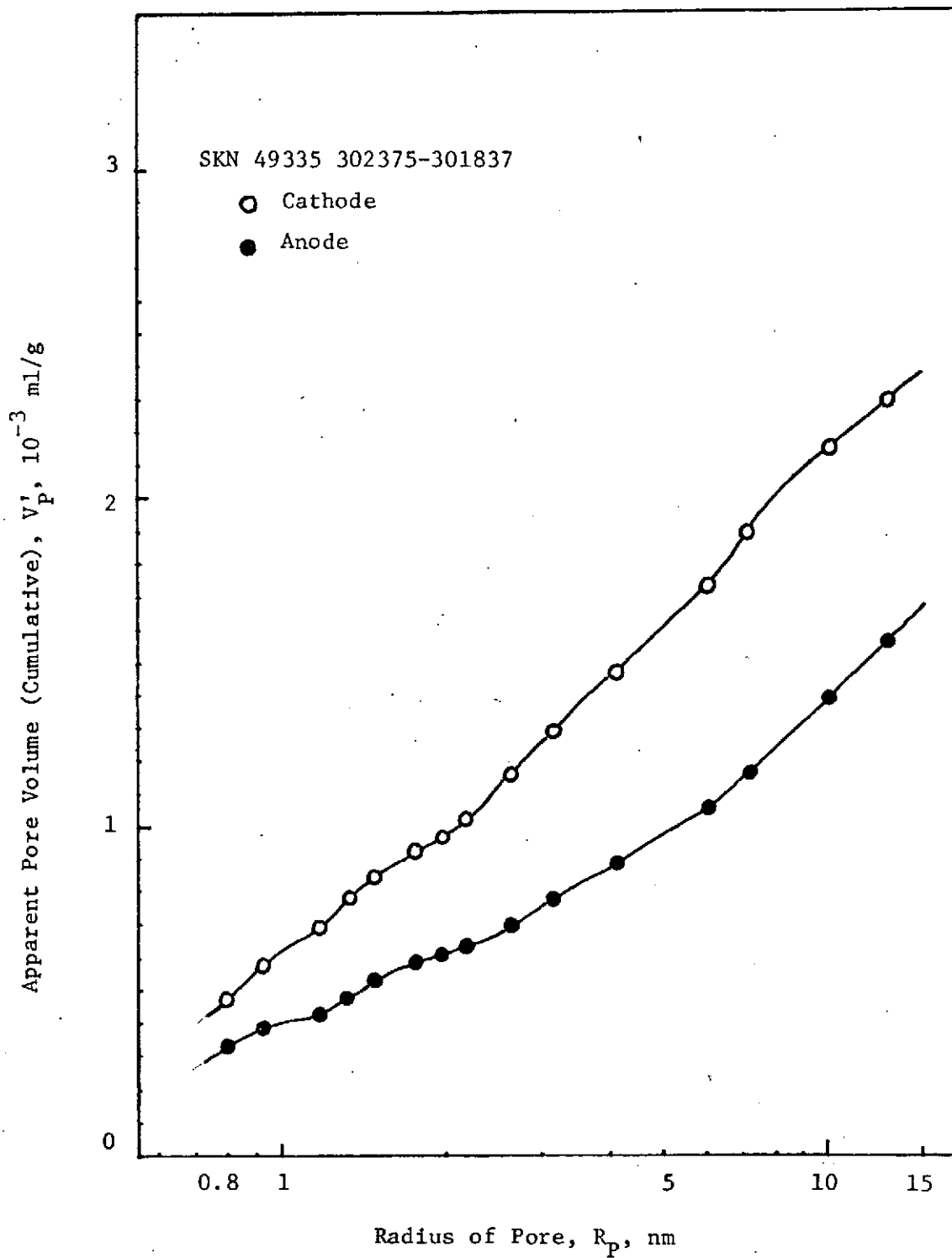
Figure 13

Pore Size Distribution of Electrode SKN 49335 302375-301837

can we tell whether it is due to the presence of CO_2 (and a reduced alkalinity) or to the presence of the PKT. The former seems the more likely cause, but experiments to examine the phenomenon would be required to clarify the point.

The pore size distribution data shown in Figures 9-13 reveal that there are several preferred pore sizes (really equivalent pore sizes since the pore radius, R_p, is calculated from the Kelvin equation on the assumption that the pore can be represented as a cylinder of uniform circular cross-section). This is not surprising as the original catalyst crystallites have been shown by electron microscopy to be grouped together in various sized clusters. All of the electrodes seem to have a preferred pore diameter of about 2.5 - 3.0 nm, which is only slightly smaller than the average crystallite size of about 6 - 7 nm (60 - 70 A). Other preferred equivalent pore diameters which are generally multiples of 2.5 - 3.0 nm are apparent from the pore size distribution curves. Since these curves clearly show that more than one population of pores exists, the usual procedure of calculating one average pore diameter was not followed. Rather, a computer program was developed to analyze the pore size distribution data and to calculate the most probable preferred equivalent pore diameters. This computer program and the results of the analysis are discussed in the next section of this report (but the data analyzed there are not for the electrodes whose pore size distribution are shown in Figures 9 - 13).

4.2.2.2 Computation of Pore Size Distribution

It may be recalled that in the nitrogen adsorption technique for measurement of pore volume one measures the amount of nitrogen adsorbed

at several relative partial pressures, P/P_o, and calculates the volume

as a liquid; then by using the Kelvin equation the equivalent pore

radius at which condensation would take place is calculated; thus, one

obtains cummulative pore volume, V, versus equivalent pore radius, R_p,

data. With the mercury penetration technique one measures the volume

of mercury which can be forced into the pores of the material under

investigation at various increasing pressures P; then one calculates

corresponding pore radius R_p using the equation

$$P \; R_p \; = \; -2 \; \sigma \; \cos \; \Theta \tag{4}$$

where σ is the surface tension of mercury, and Θ is the contact angle

between mercury and the material under study.

Usually, it is assumed that there is one population of pores and

a single mean pore radius is calculated, but it was clear from both our

data and electron micrographs (Figures 7 and 8 of the Fourteenth Semi-

annual Report) that we had more than one preferred equivalent pore

radius. To derive a more realistic pore size distribution for such

multiple population data one needs to know the distribution function

$L(R)$ as defined later and its modes. A computer program was developed

to find modes of the distribution function and obtain the mean radius

and standard deviation.

Owing to the time involved one usually gets pore volume data at

10 - 15 points over the range of relative pressures (in the case of BET)

or applied pressures (in the case of mercury penetration). In order

to get a finer grid, we generate additional "experimental" points.

The program first searches n + 1 points around the desired point

R_i in the $\underline{R}$ vector of argument points and gives a corresponding

interpolated function value of V_i using a polynomial of nth order

(we used 4th order) by the Aitken-Lagrange interpolation technique (2).

In order to give equal weight to all experimental points an equal number

of points, IDT, are generated between two experimental points rather

than generating equidistant points. Thus, if we had N experimental

points to start with we obtain total of M points where

$$M = IDT\ (N - 1) + 1 \tag{5}$$

From the vector $\underline{R} = (R_1,\ \ldots\ R_M)$ of argument values and the vector

$\underline{V} = (V_1,\ \ldots,\ V_M)$ of corresponding function values we then compute a

vector $\underline{\dot{V}} = (\dot{V}_1,\ \ldots\ \dot{V}_M)$ of derivative values, dV/dr, using the

Lagrangian interpolation polynomial of degree 2, relevant to three

successive points. Note that one obtains $\left.\dfrac{dV}{dr}\right|_R$, i.e., volume occupied by

pores having diameters between $(R - 0.5)$ to $(R + 0.5)$. Since we are

interested in a number frequency of such pores having unit length we first

obtain the total length of such pores by dividing the differential pore

volume $\left.\dfrac{dV}{dr}\right|_R \cdot \Delta R$ (where $\Delta R = 1.0$) by an average cross-sectional area,

πR^2. This gives the numerical value of the distribution function, $L(R)$,

of pores of unit length, $L = 1$, and diameter R.

$$L(R) = \frac{\left.\dfrac{dV}{dr}\right|_R}{\pi R^2} \qquad \left[\begin{array}{l} \text{and} \quad L = 1 \\ \quad\quad\ \Delta R = 1 \end{array}\right] \tag{6}$$

A search for mode involves a search for local minima and maxima of

the distribution function $L(R)$. In order to eliminate noise in the search

certain criteria were chosen for valid minima and maxima: (1) each

valid maximum should be followed by at least three points that are

lower than the value of the maximum itself; (2) each valid minimum

should be smaller than 70% of the immediately preceeding maximum and

should be followed by at least three points that have higher value than

this minimum; and (3) both endpoints are always counted as minima.

If we obtain $m + 1$ number of minima, we have m populations of m preferred equivalent pore radii. A mean pore radius is calculated for each of these populations between two successive minima, Min (j) and Min (j + 1) where $j = 1, \ldots, m$.

$$\bar{R}_j = \frac{\sum_i L(R_i) R_i}{\sum_i R_i} \tag{7}$$

and

$$\sigma_j^2 = \frac{\sum_i L(R_i) R_i^2 - \left[\sum_i L(R_i) R_i \right]^2 / \sum_i L(R_i)}{\sum_i L(R_i) - 1} \tag{8}$$

In these equations the summations are carried out for values of i lying between two successive minima.

The results of such calculations on several samples are shown in Table 3 and compared with the overall mean pore radius, $< R >$, calculated by:

$$< R > = \frac{\int_0^V r \, dV'}{\int_0^V dV'} \tag{9}$$

For this purpose R vs V' data are best fitted to a polynomial of degree up to 10 (if necessary) to get

$$R = P(V') \tag{10}$$

and analytical integration yields $< R >$. From the tabulated results it is very clear that the overall mean pore radius is of little value for characterizing electrode materials.

Table 3

Computer Analysis of Pore Size Distribution of Fuel Cell Electrodes

Englehard Fuel Cell Platinum		P & W Fuel Cell Anode Strip Cell SCD No. 2		P & W Fuel Cell Cathode Strip Cell SCD No. 2	
Local Maxima	Mean Radius and Std. Dev.	Local Maxima	Mean Radius and Std. Dev.	Local Maxima	Mean Radius and Std. Dev.
1.9 nm*	3.1 ± 1.5 nm	1.9 nm	2.2 ± 0.51 nm	1.9 nm	1.94 ± 0.25 nm
–	–	–	–	2.9	3.24 ± 0.63
–	–	4.2	4.46 ± 0.87	5.0	5.62 ± 0.76
–	–	6.6	6.64 ± 0.41	–	–
7.9	8.21 ± 0.73	7.9	9.13 ± 1.22	7.9	8.68 ± 1.08
11.6	11.54 ± 1.13	12.6	12.56 ± 0.64	11.6	12.04 ± 0.87
14.7	17.76 ± 37.2	14.7	18.23 ± 4.02	14.7	18.17 ± 3.75

Mercury Penetration Measurements

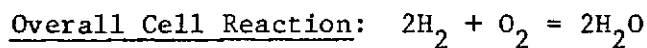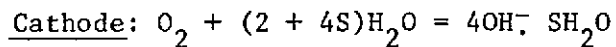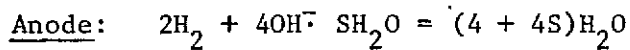| None	None	1.8 nm	1.8 ± 0.07 nm	2.1 nm	2.0 ± 0.15 nm
		2.5	2.5 ± 0.2	–	–
		–	–	4.2	4.0 ± 0.26
		13.8	14.8 ± 3.7	10.5	14.0 ± 4.8
		93.9	101.6 ± 17.7	–	–
		240	250 ± 30	–	–
		980	1300 ± 800	700	640 ± 240
		7700	8200 ± 1000	6500	8800 ± 4400
		12900	16600 ± 7700	–	–

Overall Mean Pore Radius From BET Measurements

13.5 nm	15.24 nm	15.17 nm

* 1000 nm = 1 µm

5. Water Transport In Fuel Cells--S. P. Lui

It is common practice to write electrode and overall cell reactions
as though the solvent did not exist. However, in the alkaline H_2-O_2
fuel cell it is important to take the solvent, water, into account, not
only because it is a reactant at the cathode but because water is consumed
in solvating the hydroxyl ions which are the cathode reaction product.
Thus, it seems desirable to write the electrode and overall cell reactions
in the following manner,

Anode: $2H_2 + 4OH^- \cdot SH_2O = (4 + 4S)H_2O$

Cathode: $O_2 + (2 + 4S)H_2O = 4OH^- \cdot SH_2O$

Overall Cell Reaction: $2H_2 + O_2 = 2H_2O$

It is clear from an examination of these reactions that $(2 + 4S)$ moles
of H_2O must diffuse from the anode to the cathode per mole of O_2 reacting
at the cathode to supply the water requirement there, while 2 moles of
water (the net cell reaction product) must be rejected from the cell.
Moreover, it is obvious that the water required at the cathode is doubled
if the hydration number of the hydroxyl ion is unity, and that the cathode
water requirement increases rapidly as the hydration number increases
(we can ignore the hydration number of the potassium ion for the moment
because potassium ions do not enter into the electrode reaction). Thus,
if one ignores hydroxyl ion solvation, the cathode water requirement is
only 2 moles of H_2O/mole O_2, while if $S_{OH^-} = 1$, the cathode water requirement
is 6 moles of water per mole of O_2 reacting; if $S_{OH^-} = 3$, the cathode
water requirement is 14 moles of water per mole of O_2 reacting. It
should be noted that each hydroxyl ion moving from the cathode to the
anode (by a combination of diffusion and electromigration) carries with

it S molecules of bound water, all of which must be returned to the cathode by diffusion when the fuel cell is operating at steady-state. Thus, we have "free" water diffusing from the anode to the cathode and "bound" water moving from the cathode to the anode.

When one thinks in terms of current densities and reaction rates, however, the cathode water requirement may be even larger because at high current densities it is clear that the hydroxyl ion concentration at the cathode may increase. To preserve electroneutrality, potassium ions must move into the cathode and transient effects may occur. We shall not concern ourselves with transient behavior at this time; rather we shall restrict our attention to steady-state conditions.

5.1 General Transport Equations

In concentrated solutions, the flux of each species is given by

$$c_i \nabla \mu_i = RT \sum_j \frac{c_i c_j}{c_T \mathscr{D}_{ij}} (\underline{v}_j - \underline{v}_i) \tag{11}$$

The fluxes of K^+, OH^- and water in a concentrated solution of KOH are as follows:

$$N_+ = c_+ \underline{v}_+ = - \left[\frac{v_+ \mathscr{D} c_T}{\nu RT} \frac{c_T}{c_0} c \right] \nabla \mu_e + \frac{t_+^0 i}{z_+ F} + c_+ \underline{v} \tag{12}$$

$$N_- = c_- \underline{v}_- = - \left[\frac{v_- \mathscr{D} c_T c}{\nu RT c_0} \right] \nabla \mu_e + \frac{t_-^0 i}{z_- F} + c_- \underline{v} \tag{13}$$

$$N_{H_2O} = c_0 \underline{v} - D \nabla c_0 \tag{14}$$

where

$\nu = \nu_+ + \nu_-$ is the number of moles of ions into which a mole of electrolyte dissociates.

$\mathscr{D}$ = diffusion coefficient of electrolyte, based on thermodynamic driving force.

D = measured diffusion coefficient.

c = molar concentration of KOH, mole/cm^3.

c_o = concentration of water.

c_T = total solution concentration

= $c + c_o$

t_+^o = transference number of K$^+$ with respect to the velocity of water.

t_-^o = transference no. of OH$^-$.

z_i = charge number

$\underline{v}$ = mass-averaged velocity cm/sec

μ_e = chemical potential of KOH J/mole.

The gradient of chemical potential is given by:

$$\nabla \mu_e = \left(\frac{\nu RT \, c_o}{\mathscr{D} c_T} \right) D \left[1 - \frac{d \ln c_o}{d \ln c} \right] \nabla c \tag{15}$$

Hence Equations (12), (13) and (14) become:

$$N_+ = -\nu_+ D \left[1 - \frac{d \ln c_o}{d \ln c} \right] \nabla c + \frac{i t_+^o}{z_+ F} + c_+ \underline{v} \tag{16}$$

$$N_- = -\nu_- D \left[1 - \frac{d \ln c_o}{d \ln c} \right] \nabla c + \frac{i t_-^o}{z_- F} + c_- \underline{v} \tag{17}$$

$$N_{H_2O} = c_o \underline{v} - D \nabla c_o \tag{18}$$

Let us consider the case where $\underline{v} = 0$. We can then write

$$c_o = c_T - c \tag{19}$$

$$\frac{dc_o}{dx} = -\frac{dc}{dx} \tag{20}$$

$$N_{H_2O} = -D\frac{dc_o}{dx} = -D\left(-\frac{dc}{dx}\right) = D\frac{dc}{dx} \tag{21}$$

Since in the alkaline $H_2 - O_2$ fuel cell potassium ions do not enter into the reaction, we can write

$$N_+ \doteq 0 \tag{22}$$

from which we can deduce that

$$N_{H_2O} \doteq -N_- \tag{23}$$

or

$$D\frac{dc}{dx} = -\left\{-\nu_- D\left[1 - \frac{d\ln c_o}{d\ln c}\right]\frac{dc}{dx} + \frac{it_-^o}{z_-F}\right\} \tag{24}$$

This leads to

$$N_{H_2O} = D\frac{dc}{dx} = \nu_- D\left(1 - \frac{d\ln c_o}{d\ln c}\right)\frac{dc}{dx} - \frac{it_-^o}{z_-F} \tag{25}$$

From Equation 25, we see that the flux of water depends on several parameters; among them are the transference number of hydroxide ions, t_-, the concentration of water in the solution, c_o, and the diffusivity of water in the solution, D. All of these parameters are strongly concentration-dependent. The diffusivity of water in KOH solutions has been measured by Bhatia (3), but knowledge concerning the transference number of hydroxyl ions in concentrated KOH solutions is meager. The ions in KOH solutions are hydrated, and the concentration of free water in the solution clearly depends on the hydration number. Since information on both the transference numbers and hydration numbers of ions in concentrated KOH solutions is limited, the small amount of time available during this reporting period was devoted to a literature survey on subjects. These studies are summarized in the sections following.

5.2 Transference Number of Potassium Ion in KOH Solutions

The transference number of an ion is defined as the fraction of the total current which is carried by that ion. Transference number measurements, when used in conjunction with conductivity measurements, enable one to calculate the mobilities of the individual ions.

In 1923, Knobel (4) calculated the transference number of the potassium ion by measuring the EMF of cells containing the same KOH solutions, with and without transference. He found that the transference number of potassium ion was 0.2633, and that it was independent of KOH concentration over the concentration range from 0.03 N to 3.0 N.

The transference number may also be expressed as

$$t_i = \frac{\lambda_i}{\Lambda} \tag{26}$$

where the ionic conductance, λ_i, and the equivalent conductance of the solution, Λ, are different at different concentrations. Thus, the transference number may not necessarily be a constant. According to the Onsager equation,

$$\lambda_i = \lambda_i^o - \left[\theta \lambda_i^o + \frac{1}{2} \sigma \right] \sqrt{c} \tag{27}$$

where θ and σ are constants, the transference number of potassium ion decreases as the concentration of the KOH solution increases and at infinite dilution the transference number of the potassium ion is 0.271.

Although dilute electrolyte solutions have been studied intensively, studies in concentrated solutions have been much less frequent; and while the Onsager theory predicts the concentration-dependence of the transference number, it is applicable only at low concentrations. Attempts to extend the Onsager equation to higher concentrations have not met with success.

Recently, Merenkov (5) measured the transference number of potassium ions in KOH solutions ranging in concentration from one to ten equivalents per liter. He found that the transference number of potassium ion was independent of temperature from 18° to 65°C but that it decreased with increase in KOH concentration. The transference number of potassium ions was correlated satisfactorily by the empirical equation

$$t_{K^+} = 0.26 - 0.047 (\sqrt{c} + 1) \tag{28}$$

The results of Knobel, Onsager, and Merenkov are summarized in Table 4.

The experimental results obtained by Knobel do not agree with the theoretical results obtained by using the Onsager equation. Jones, et al. (6) have shown that for barium chloride and lithium chloride solutions, the transference number for the cations decreases with increase in concentration. Hence the results obtained by Knobel may not be very reliable.

In fuel cell operations, we are dealing with concentrated solutions of KOH. The use of the Onsager equation almost certainly leads to erroneous results. The empirical equation proposed by Merenkov, though, gives the concentration dependence of the transference number, yet the value at infinite dilution as predicted by this empirical equation is 0.213 which is far below the theoretical value of 0.271, a value on which both Knobel and Onsager agree. At a concentration of 1 N, the transference number of the potassium ion calculated by using the empirical equation obtained by Merenkov is 0.166. The result obtained by using the Onsager equation is 0.158. Thus, the Merenkov equation appears to be suitable for KOH concentrations above 1.0 N.

5.3 The Primary Hydration Number of Potassium and Hydroxide Ions

It is obvious that ions in a solution are solvated, but this fact

TABLE 4

Summary of Transference Number Data For KOH Solutions

Concentration of KOH solution (n)	Transference number of K^+ from		
	Knobel eq.	Onsager eq.	Merenkov eq.
0	–	0.271	0.213
0.03	0.2633	0.259	0.205
0.1	0.2633	0.248	0.198
0.3	0.2633	0.226	0.187
1	0.2633	0.158	0.166
3	0.2633	–	0.132
4	–	–	0.119
7	–	–	0.088
10	–	–	0.064

receives little attention in most discussions. In concentrated solutions

hydration can no longer be ignored. Hydration is somewhat arbitrarily

pictured in terms of primary and secondary hydration sheaths, in a

manner similar to descriptions of uneven charge distributions at the

electrode/electrolyte interface. Water in the primary hydration sheath

is viewed as being so tightly bound to the ion that it moves with the

ion, whereas water in the secondary hydration sheath is considered to

be so loosely bound that it is in continual exchange with the surrounding

medium. As a first approximation, it seems reasonable to consider only

the primary hydration sheath as it might influence the behavior of fuel

cells.

Although the solvation number of ions has been discussed by several

investigators, the most recent and most applicable paper seems to be that

of Bockris and Saluja (7). These authors related the solvation number of

an ion to its ionic radius. Using ionic radii taken from Wyckoff (8)

and the graphs given in the Bockris and Saluja paper, one can estimate

that the hydration number of the hydroxyl ion, S_{OH^-}, is 4.5 while that

of the potassium ion, S_{K^+}, is 3.5. An experimental value for fluoride

ion (which is about the size of the hydroxyl ion) is $S_{F^-} = 4.0$. When

one examines the literature, however, the hydration numbers reported

for potassium ion range from about 2 to 6 or more, and it seems clear

that the values of the hydration number derived above are not at all

precise. Moreover, even if we assume that the hydration number of both

the potassium and hydroxyl ions is the same, i.e., about 4, we have a

problem in that there is not sufficient water in 30 wt. percent KOH to

provide 4 water molecules for each potassium and each hydroxyl ion. The

density of 30 wt % KOH solution is 1.29 g/ml and we can calculate the KOH

concentration to be

$$C_{KOH} = \frac{30 \text{ g KOH/100 g soln x } 1.29 \text{ g soln/ml x } 1000 \text{ ml/l}}{56.1 \text{ g KOH/g. mole}} = 6.9 \frac{\text{g mole KOH}}{\text{l. soln}}$$

The molar concentration of water is

$$C_{H_2O} = \frac{(100 - 30) \text{ g H}_2O/100 \text{ g soln x } 1.29 \text{ g soln/ml x } 1000 \text{ ml/l}}{18 \text{ g H}_2O/\text{g. mole}} = 50.$$

$$= 50.2 \frac{\text{g. mole H}_2O}{\text{l. soln}}$$

If the hydration number can be considered to be the same for both potassium and hydroxide ions, we can calculate the concentration of "free" water, i.e., the water not tightly bound in the primary hydration sheaths of the ions and apparently free to diffuse as follows:

$$C_{FW} = C_{TW} - C_{BW} = C_{TW} - 2SC_{KOH} \qquad (29)$$

where C_{FW} = concentration of "free" water

C_{TW} = concentration of total water

C_{BW} = concentration of bound water

C_{KOH} = concentration of KOH

For example if $S_{K^+} = S_{OH^-} = 1$,

$$C_{FW} = 50.2 - (2)(1)(6.9) = 50.2 - 13.8 = 36.4 \text{ g moles/l.}$$

A plot of the concentration of "free" water versus the KOH concentration is shown in Figure 14 for several values of the hydration number. From this graph, several conclusions can be drawn. In the first place, the maximum hydration number permissible in 30 wt% KOH is about 3.5 (again assuming $S_{K^+} = S_{OH^-}$). Also, since the solubility limit of KOH in water at 25°C is about 55 wt% KOH, an average hydration number of about one

Figure 14 - Concentration of Free Water in KOH Solution
For Different Degree of Solvation.
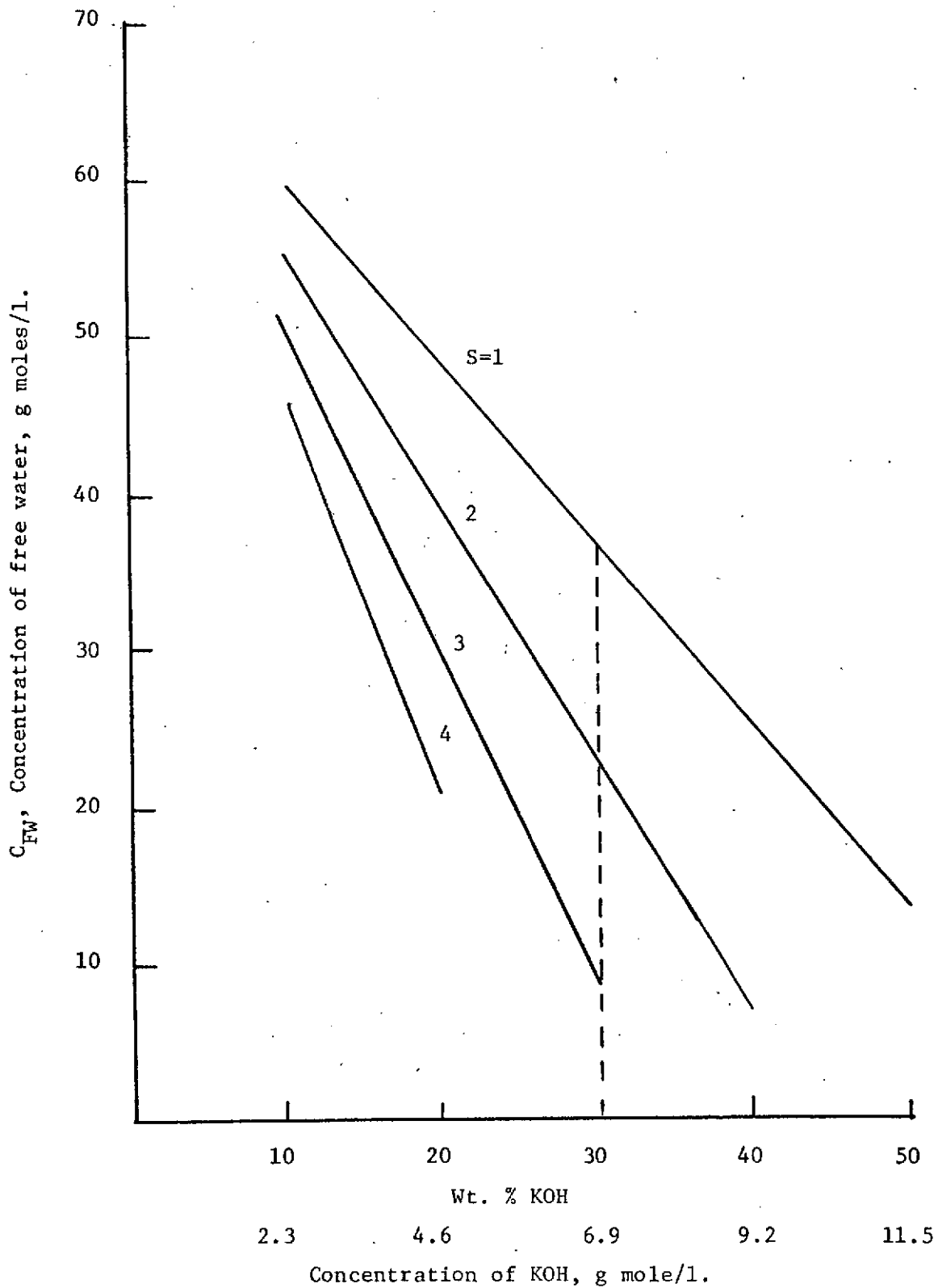
must be applicable for very concentrated solutions. Since 30 wt % KOH
is only about half saturated, and the hydration number in very dilute
solutions appears to be around 6, a hydration number of 2 to 3 seems
reasonable for 30 wt % KOH.

6. Wetting and Penetration In Fuel Cell Components - H. Lathanh

Although normally the interstices of the electrolyte matrix in a fuel cell are filled with electrolyte and only the "wet-proofed" electrodes are partially filled, wetting and penetration of the electrolyte into the interstices or pores of any fuel cell component is important for the stability of the gas/liquid interface, particularly if local instabilities develop for any reason. In the limited time available for this task during this reporting period it was not possible to do anything more than review the literature for information on the surface tension of KOH solutions.

The surface tension of KOH solutions is given in the International Critical Tables (9) for temperatures of 15 - 18°C and KOH concentrations up to 17.5 wt. percent. Röntgen and Schneider (10) also reported the surface tension of KOH solutions. These data agree very well; they are shown in Figure 15. Faust (11) also studied the surface tension of KOH solutions up to a KOH concentration of 28.4 wt. percent. He showed a greater concentration dependence at the higher KOH concentrations than an extrapolation of the ICT would predict. Faust's data are also plotted on Figure 15.

No surface tension data are available for higher KOH concentrations and higher temperatures.

In view of the lack of surface tension data at high KOH concentrations and higher temperatures measurements will be undertaken at the earliest opportunity. In addition contact angle measurements on heterogeneous, porous surfaces will also be undertaken in an effort to understand wetting and penetration of "wet-proofed" electrodes.
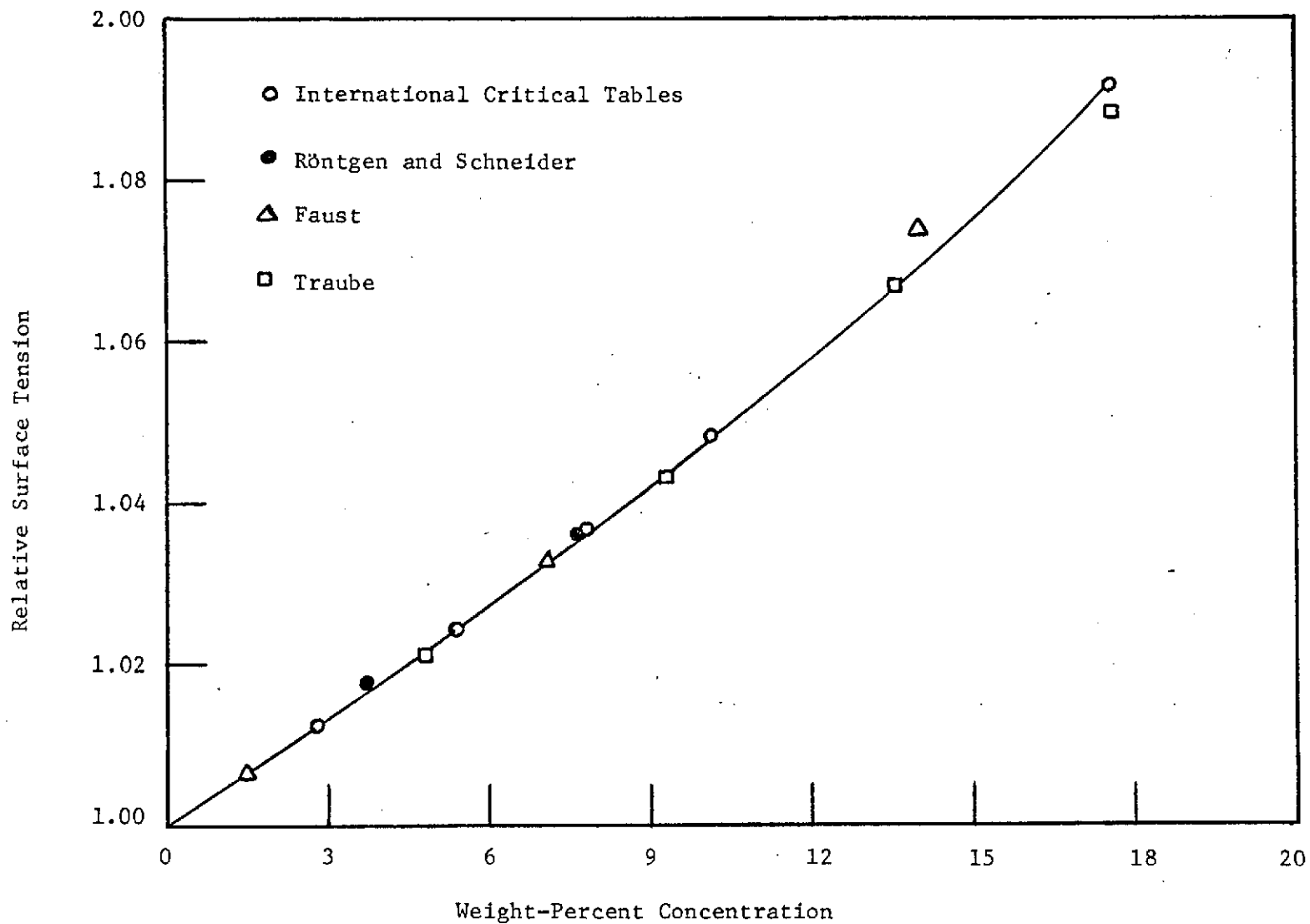
Figure 15:   Surface Tension of KOH Solutions

LIST OF REFERENCES

1. Wood, K. O. and Ball, W. F., Final Report, NASA Contract No. CR-72906, Pratt & Whitney Aircraft Division, United Aircraft Corp., Feb., 1971.

2. F. B. Hildebrand, "Introduction to Numerical Analysis", McGraw-Hill, New York, 49-50 (1956).

3. Bhatia, R. N., M.S.E. Thesis, University of Florida (1968).

4. Knobel, M., J. Am. Chem. Soc., 45, 70 (1923).

5. Merenkov, P. T., Uzbeksk. Khim. Zn., 1961, No. 4, 50-7.

6. Jones, G. and Dole, M., J. Am. Chem. Soc., 51, 1073 (1929).

7. Bockris, J. O'M., and Saluja, P. P. S., J. Phys. Chem., 76, 2140 (1972).

8. Wyckoff, R. W. G., "The Structure of Crystals", p, 192. Reinhold Publishing Corp., New York (1931).

9. International Critical Tables, 1st Ed., IV, 466 (1928).

10. Röntgen, W. C., and Schneider, J., Ann. des Phys. Und Chem., 29, 165 (1886).

11. Faust, V. O., Zert. Anorg. Chem., 160, 373 (1927).